

Interaction at a Distance: Xenon Migration in Mb

Haydar Taylan Turan, Eric Boittier and Markus Meuwly*

*Department of Chemistry, University of Basel, Klingelbergstrasse 80 , CH-4056 Basel,
Switzerland.*

E-mail: m.meuwly@unibas.ch

Abstract

The transport of ligands, such as NO or O₂, through internal cavities is essential for the function of globular proteins, including hemoglobin, myoglobin (Mb), neuroglobin, or truncated hemoglobins. For Mb, internal cavities Xe1 through Xe4 were observed experimentally and they were linked to ligand storage. The present work determines barriers for xenon diffusion and relative stabilization energies for the ligand in the initial and final pocket linking a transition depending on the occupation state of the remaining pockets from both biased and unbiased molecular dynamics simulations. It is found that the energetics of a particular ligand migration pathway may depend on the direction in which the transition is followed and the occupation state of the other cavities. Furthermore, the barrier height for a particular transition can depend in a non-additive fashion on the occupation of either cavity A or B or simultaneous occupation of both cavities, A and B. Multiple repeats for the Xe1→Xe2 transition reveal that the activation barrier is a distribution of barrier heights rather than one single value which is confirmed by a distribution of transition times for the same transition. Dynamic cross correlation maps demonstrate that correlated motions occur between adjacent residues or through space, residue Phe138 is a gate for the Xe1→Xe2 transition, and the cavity volumes vary along the diffusion pathway, indicating that there is dynamic communication between the ligand and the protein. The sum of these molecular-level analyses suggests that Mb is an allosteric protein.

1 Introduction

Proteins can contain cavities which play potentially functional roles as they allow transient ligand localization and transport between neighboring sites. Although cavities have been traditionally regarded as “packing defects” that can destabilize a protein structure¹ they are quite ubiquitous. Directly mapping out such cavities has been possible for a number of proteins, including myoglobin (Mb),² Cytochrome ba3 Oxidase,³ T4 lysozyme,⁴ or interleukin-1 β .⁵ For T4 Lysozyme cavity-creating mutations by replacing various amino acids

by alanine were found to decrease the thermodynamic stability of the protein by 2.7 kcal/mol to 5.0 kcal/mol.⁶ For azurin similar experiments were carried out which also indicated that thermodynamic stability is decreased upon replacement of wild type residues by alanine.⁷ Additional analysis revealed that there is no correlation between thermodynamic stability and flexibility which may be related to the particular modification sites chosen. Finally, for hen egg white lysozyme cavity filling mutations were explored for which the Met12Phe mutant was found to be more stable than the WT protein by 0.8 kcal/mol.⁸ More recently, cavities were also designed “de novo” from computer modeling and confirmed by X-ray crystallography with the largest such cavity measuring 520 Å³.⁹

In addition to cavities as ligand binding positions within a protein, such cavities can also be part of a ligand storage and diffusion network such as for myoglobin or truncated Hemoglobin (trHb),^{10,11} neuroglobin (Ngb),^{12–15} or cytoglobin (Cyt).¹⁶ For myoglobin, four xenon binding sites (Xe1 to Xe4) in addition to the main binding site (usually referred to as “A” for bound and “B” for unbound ligand) at the heme-iron were characterized experimentally.² The physiological relevance of individual sites has been discussed in the literature and indicates that blocking sites “B” and/or “Xe4” have profound physiological consequences for the overall rates of O₂ binding to Mb.¹⁷ Filling the main binding site by suitable mutations lowers the rates of both ligand recruitment and dissociation. Furthermore, in a comprehensive mutagenesis study, the Xe4 cavity was filled by inserting Trp at strategic positions. Such mutations block access of the ligand to the protein interior. This leads to increased geminate recombination. However, it was also reported that the rate of ligand entry is modulated by Trp mutations in the “B” and in Xe4 pockets. Hence, the size of the distal pocket plays a central role for ligand entry and capture and the two processes appear to be concerted on the μ s and ms time scales.¹⁷ Blocking the Xe1 site was also studied by either adding Xe gas or by mutation of L89, L104, or F138 to Trp.¹⁸ There is little change in the total fraction of geminate recombination but all these modifications markedly reduce the amplitude of the

slower recombination phase,¹⁸ possibly due to rigidification of the iron-out-of-plane motion which gates ligand rebinding.¹⁹

While xenon as a ligand to myoglobin does not have a biological function it is often used as a convenient probe to map out internal cavities.^{2,3,20} This is also what xenon is used for in the present work. For proteins with multiple internal binding pockets the question arises whether and in what way ligand migration pathways depend on the internal occupation state. In other words, the question is whether for a transition between cavities A and B the occupation state of cavity C (empty or filled) affects the barrier that needs to be overcome. Depending on the answer to this question, important implications result for protein function and protein design. As mentioned above, occupation of Xe1 has been found to markedly reduce the amplitude of the slower recombination rate of a ligand at the main binding site. Hence, it is expected that a more comprehensive assessment of the influence of internal occupation state (by physically placing a ligand - here xenon - or by mutation to partially or entirely fill an internal site) will provide further information about the relationship between cavity occupation and migration pathways and associated energetics.

The term “allostery” - Greek for “other site” - used with reference to molecular-level control of cellular function, was introduced in 1961 to describe “interaction at a distance” involving two (or multiple) binding sites in a protein.²¹ However, the concept is older than that, going back to Pauling for explaining positive cooperativity in binding of molecular oxygen to Hemoglobin.²² This model eventually developed into the “Koshland-Nemethy-Filmer” (KNF)²³ as opposed to the model by “Monod, Wyman and Changeux” (MWC) which provided an alternative view of allostery. When applied to oxygen binding to hemoglobin, the MWC involves only changes at the quaternary structural level whereas KNF is only concerned with tertiary structural changes. Allostery is also a fundamental regulatory mechanism that plays a role in various biological processes such as gene regulation,²⁴ signal transduction,²⁵

and metabolism.²⁶ Ligand binding is one of the important “perturbations” that causes allosteric regulation. Previous models of allostery, such as KNF and MWC, were based on crystallographic observations and were limited in focus to perturbations at the tertiary and quaternary structural level.^{27–29} Due to advancements in NMR spectroscopy,³⁰ alongside developments in molecular dynamics (MD) simulation,^{31–33} insights into allosteric regulation induced by ligand binding at the molecular level have emerged. These approaches have benefited from enhanced sampling methods in MD, as well as graph-based community and network detection algorithms which have been shown to be effective at identifying important residues and transition pathways to further the understanding of allostery at a molecular level.^{32,34}

The present work is structured as follows. First, the computational methods including the MD simulations and their analysis is presented. This is followed by a discussion of the migration energetics for Xe depending on the occupation state of the remaining cavities. Next, the correlated motions within Mb are characterized and volume changes of the pockets are analyzed. Finally, the results are discussed in a broader context of allostery and conclusions are drawn.

2 Computational Methods

2.1 Molecular Dynamics

All molecular dynamics (MD) simulations were performed using the CHARMM³⁵ software with CHARMM22 force field, with $R_{\min} = 2.05 \text{ \AA}$ and $\epsilon_{ij} = -0.42 \text{ kcal/mol}$ for the Xe atom. This radius is somewhat smaller than the one used previously ($R_{\min} = 2.24 \text{ \AA}$ ³⁶). Myoglobin (Mb) was placed in the center of the solvent box with dimensions $65.2 \times 59.0 \times 46.6 \text{ \AA}^3$, and maintained there with a 1 kcal/mol center of mass constrain. MD simulations were started

following 500 steps of steepest descent and 500 steps of Adopted Basis Newton-Raphson minimization then the system was heated to 300 K and equilibrated for 50 ps in *NVT* ensemble. Then, 1 ns of *NVE* was carried out with leapfrog integrator³⁷ using a time step of $\Delta t = 1$ fs, and all bonds involving hydrogen atoms were constrained using SHAKE.³⁸ Non-bonded interactions were treated with a switch function³⁹ between 12 and 16 Å. Xe atoms not involved in transitioning between neighboring pockets are retained in their given pockets by a harmonic constrain with a force constant of 10 kcal/mol.

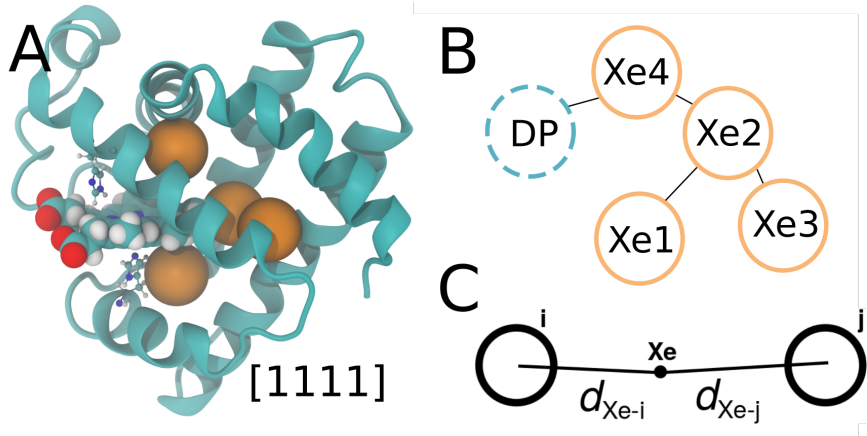


Figure 1: Panel A. The structure of myoglobin with four internal pockets (Xe1 - Xe4) occupied with xenon atoms (orange spheres). Panel B. An idealized graph showing possible migration pathways between pockets, including the distal pocket (DP), which are investigated using umbrella sampling. Panel C. Definition of the reaction coordinates r_c^A and r_c^B based on d_{Xe-i} and d_{Xe-j} distances.

All simulations were initialized from an initially equilibrated fully occupied protein (1111) with pockets Xe1 to Xe4 occupied by one xenon atom each. A binary system is used in the following to identify the Xe occupation state of Mb. For example, 0100 represents Mb with Xe present in Xe2, with pockets Xe1, Xe3, and Xe4 empty, whereas 1011 represents a system in which Xe1, Xe3, and Xe4 host a Xe atom. The Xe atoms were constrained to their given pockets and the initial 1111 state was equilibrated for 2 ns in the *NVT* ensemble. From this structure, 16 different Xe occupation systems were generated, covering all possible

occupation states with regards to cavities Xe1, Xe2, Xe3, and Xe4,² see Figure 1. Each system was again heated and equilibrated for 2 ns in the *NVT* ensemble with the Xe atoms constrained to their pockets. For Xe in DP, the last structure from the umbrella simulations in given state is extracted, and equilibrated for 2 ns in the *NVT* ensemble with the Xe atom constrained in DP. The definitions for the cavities were those from prior characterizations of the Xe pockets as shown in Table 1.^{11,40-43} The Xe pockets and HEME residue in myoglobin is shown in Figure 1. The connection between pockets are labelled with black lines.

Table 1: Name of each cavity within Mb along with molecules and residues which line the pocket as defined by previous research.^{44,45}

Cavity	Molecular definition
Xe1	Leu89, His93, Leu104, Phe138, Ile142, Tyr146 and HEME
Xe2	Leu72, Ile107, Ser108, Leu135, Phe138, Arg139 and HEME
Xe3	Trp7, Thr75, Leu76, Gly80, His82, Ala134, Leu137, Phe138
Xe4	Gly25, Ile28, Leu29, Gly65, Val68, Leu69, Leu72, Ile107, Ile111
Distal pocket (DP)	Leu29, Phe46, Hse64, Val68, Ile107

2.2 Umbrella Sampling Simulations

Direct sampling of Xe atoms between neighboring pockets may be slow due to the appreciable energy barriers between the pockets (> 5 kcal/mol). Therefore, umbrella sampling (US) simulations were also used to sample the reaction pathway between the pockets. The reaction coordinate chosen include 1) the distance between the Xe atom and the center of mass of the initial pocket i (d_{Xe-i}) i.e. $r_c^A = d_{Xe-i}$ and 2) the difference of distance between the Xe and center of mass of initial pocket i (d_{Xe-i}), and distance between between the Xe and center of mass of final pocket j (d_{Xe-j}), hence $r_c^B = d_{Xe-i} - d_{Xe-j}$. Simulations were carried out for equidistant windows with $\Delta r = 0.1 \text{ \AA}$ and $k_{umb} = 25$ kcal/mol.

For discussing all transitions on the same footing, the r_c values were scaled to map r_c^A and

r_c^B to the interval $[0.0, 1.0]$, as shown in Eq. 1,

$$r_c(x) = \frac{r_c^A(x) - \min(r_c^A)}{\max(r_c^A) - \min(r_c^A)}, \quad (1)$$

and visualized in Figure 1C. In this way, the reaction coordinate begins inside the minimum of the starting pocket and extends to the minimum of the terminal pocket.

US simulations were carried out in a sequential manner for both of r_c^A and r_c^B , each window was simulated for 250 ps, and windows statistics were accumulated after equilibration for 20 ps. Statistics were merged from all windows to yield a one-dimensional potential of mean force (PMF) by using the weighted histogram analysis method (WHAM)^{46,47} with a tolerance of 0.001.

2.3 Dynamical Cross-Correlation Maps

The dynamical cross-correlation maps (DCCM) and difference dynamical cross-correlation maps^{48,49} (Δ DCCM) were calculated to quantitatively characterize the effects of Xe transition inside the protein on the dynamics using the Bio3D package.⁵⁰ Dynamic cross-correlation maps matrices and coefficients

$$C_{ij} = \langle \Delta r_i \cdot \Delta r_j \rangle / (\langle \Delta r_i^2 \rangle \langle \Delta r_j^2 \rangle)^{1/2} \quad (2)$$

were determined from the position of C α in amino acids i and j with positions r_i and r_j . Δr_i and Δr_j determine the displacement of the i th C α from its average position throughout the trajectory. One should note that DCCM characterizes the correlated ($C_{ij} > 0$) and anti-correlated ($C_{ij} < 0$) motions in a protein whereas Δ DCCM provide information about which couplings are affected by the presence of Xe atoms in a given state with respect to unoccupied protein.

2.4 Volume Analysis

The SURFNET package⁵¹ was used for detecting Mb cavities Xe1, Xe2, Xe3, and Xe4 and calculating their volumes. Two different probe size $r_{\min} = 1.2 \text{ \AA}$ and $r_{\max} = 3.5 \text{ \AA}$ were used to determine the volume of the cavities.^{41,45} The distribution of volumes, $p(V)$, and their median was determined for each US window.

3 Results

First, the potentials of mean force are discussed to provide an overview of the influence of pocket occupation on the ligand dynamics. Next, the results from unbiased simulations are presented and discussed in the context of the US simulations. Then, the global dynamics of Mb in different xenon occupation states is discussed by means of dynamical cross correlation maps. This is followed by a broader discussion linking the energetics for ligand migration with structural changes and eventually allostery in Hb.

3.1 Potentials of Mean Force Starting from Mb(1111)

Initially, all umbrella sampling simulations were started from fully occupied Mb (1111) by removing surplus Xe atoms depending on the state that was investigated. Next, all remaining Xe atoms that were not part of the transition for which US was carried out were weakly constrained to the center of mass of their respective pockets. Such a preparation will initially not be structurally adapted to the respective initial occupation state, i.e. additional structural relaxation is possible. First, the profiles following this preparation are discussed and in a next step the consequences of additional relaxation are considered.

All potentials of mean force for the different occupation states are summarized in Figure 2. From top to bottom the $\text{Xe1} \leftrightarrow \text{Xe2}$, $\text{Xe2} \leftrightarrow \text{Xe3}$, $\text{Xe4} \leftrightarrow \text{Xe2}$, and $\text{Xe4} \leftrightarrow \text{DP}$ transitions are considered for all possible occupation states for the remaining pockets. Before discussing individual transitions in some more detail a broader overview is given. It is noted that the free energy barriers for the forward and reverse direction do not need to be identical. For example, for the $\text{Xe1} \leftrightarrow \text{Xe2}$, with (1011) occupation (Figure 2D) the initial and final state are energetically equivalent but the barrier heights for the forward and the reverse process differ. Alternatively, there are transitions such as $\text{Xe4} \leftrightarrow \text{DP}$ with (1001) occupation for which the energy profiles for forward and reverse transition overlap. Also, it is noted that for certain profiles the differential stabilization of the reactant and product states can interconvert depending on the direction in which the scan is carried out, e.g. panels I and J in Figure 2.

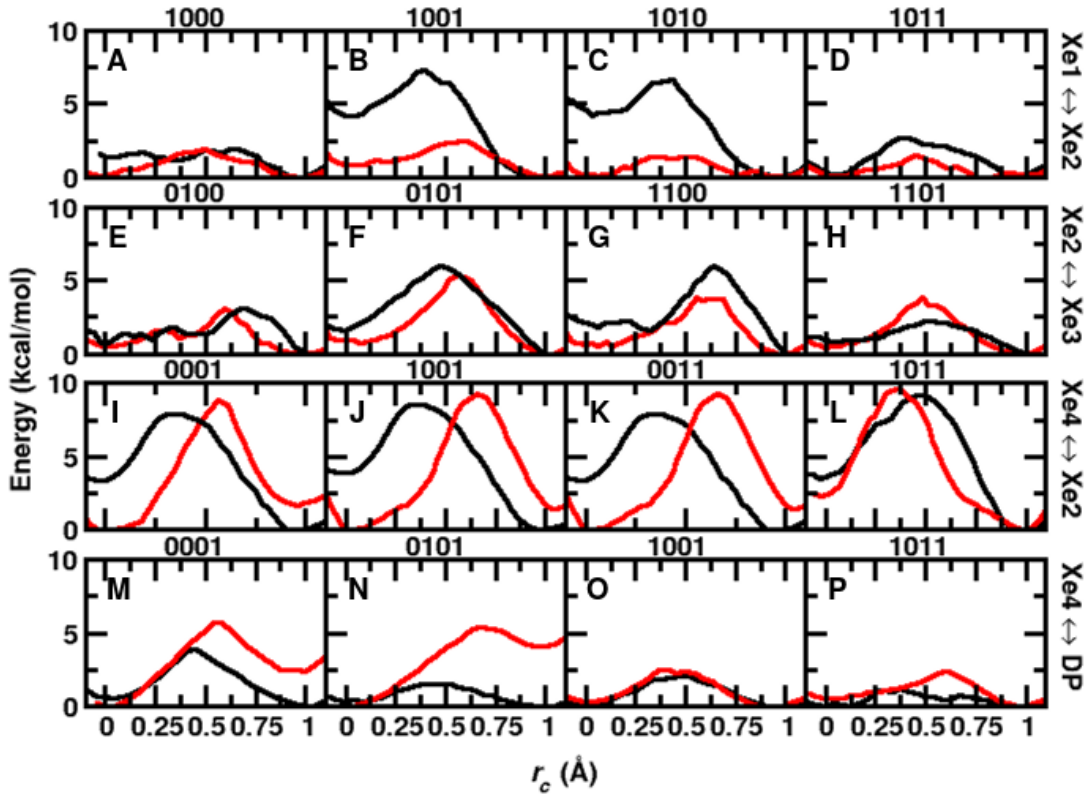


Figure 2: The PMFs for the $\text{Xe1} \leftrightarrow \text{Xe2}$, $\text{Xe2} \leftrightarrow \text{Xe3}$, $\text{Xe4} \leftrightarrow \text{Xe2}$, $\text{Xe4} \leftrightarrow \text{DP}$ transition in various systems. The forward transitions are in black and the reverse transitions are in red.

The $\text{Xe1} \leftrightarrow \text{Xe2}$ transition: For the 1000 and 1011 occupation states the stabilization energy with Xe in Xe1 and Xe2 is similar. The forward and reverse barriers, ΔG_f and ΔG_r , are comparable for 1000 but differ by ~ 0.9 kcal/mol for 1011. With 1011 occupation the activation barrier is higher ($\Delta G_f = 2.44$ kcal/mol) and earlier ($r_c = 0.35$) for the forward transition compared with the reverse transition ($\Delta G_r = 1.35$ kcal/mol and $r_c = 0.35$) whereby the initial and final states are isoenergetic, see Figure 2D. For the 1001 and 1010 occupation the energy for the state with Xe in Xe1 is higher when running the US simulation in the forward direction compared with simulations in the reverse direction.

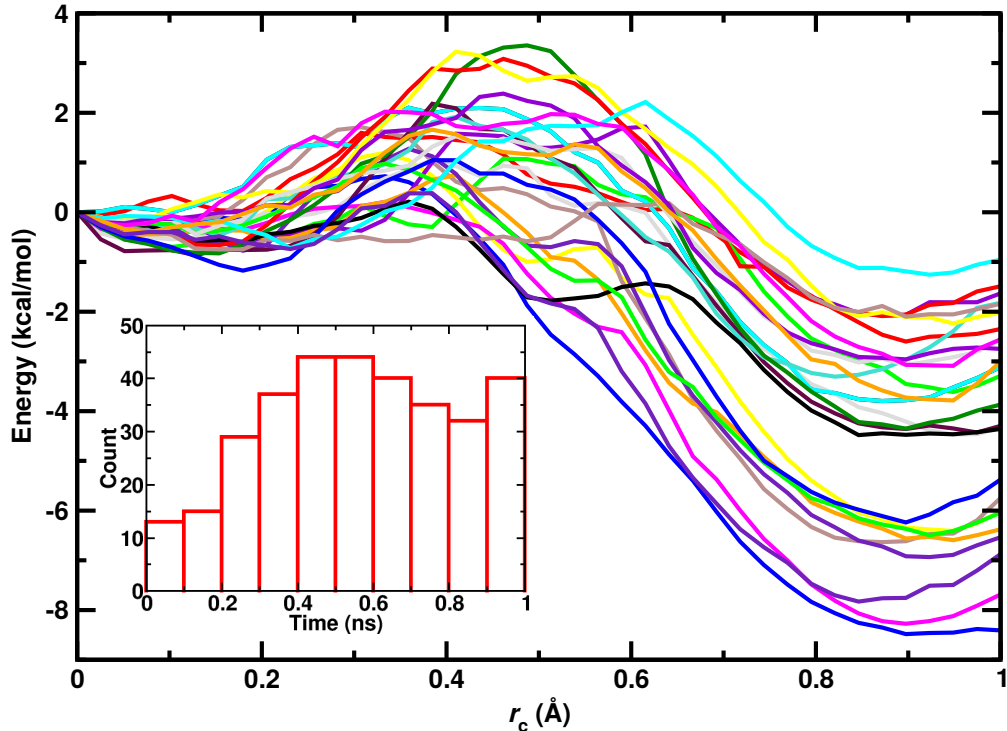


Figure 3: The PMF of the Xe1→Xe2 transition in 1001. The original PMF (black), as shown in Figure 2, is compared to the PMF for the 27 repeat simulations along the same r_c (red). Inset) The distribution of transition times for the Xe2→Xe1 transition in 0101 with bin size of 100 ps for the transition times. Overall, 2500 independent trajectories 1 ns in length were run, leading to 329 transitions.

To assess how representative the single PMFs in Figure 2 are, a larger number of independent US simulations was carried out for one specific transition in one occupation state. Repeating USs from different initial conditions for the Xe1→Xe2 transition with 1001 occupation are shown in Figure 3 and yield barrier heights ranging from 0.56 kcal/mol to 4.2 kcal/mol. From close to 30 repeats of the same US simulation the averaged forward barrier height was 2.04 ± 0.86 kcal/mol. Hence, when starting from the same initial structure but with independent initial preparation by starting the heating from a different random seed for the velocities, the barrier height (here ΔG_f) can vary appreciably. On the other hand, all profiles agree in that the structure with Xe in Xe1 is higher in energy than that with Xe in Xe2. Thus, structural heterogeneity is reflected in a distribution of Xe migration barrier heights and similar findings are expected for all other free energy profiles shown in Figure 2.

The Xe2↔Xe3 transition: For this transition and all occupation states the energy levels for the initial (Xe in Xe2) and final (Xe in Xe3) states are independent on the direction in which the transition was probed. Typically, the state with Xe in Xe2 ($r_c = 0.0$) is slightly higher in energy than for Xe in Xe3 but within the estimated accuracy of the simulations of ± 1 kcal/mol (see e.g. Figure 3), the two states can be considered isoenergetic. For the 0100 occupation, the PMF is essentially flat between Xe in Xe2 and the TS with $\Delta G_f = 1.6$ kcal/mol and $\Delta G_r = 1.8$ kcal/mol and a TS at $r_c = 0.30$ and $r_c = 0.35$ in the two directions, respectively. For 0101 the reverse barrier differs insignificantly by $\Delta\Delta G_r = 0.03$ kcal/mol for the forward and the reverse directions and the TS occurs at slightly different reaction coordinate ($r_c = 0.48$ and $r_c = 0.6$, respectively). More importantly, however, the barrier heights depend on whether pocket Xe4 is empty (0100) or occupied (0101). The difference in the free energy barrier is about a factor of two. Similarly, for 1100 the barrier heights are larger than for 0100 whereas for 1101 the barriers are more reminiscent of those of 0100 occupation. This suggests not only that the occupation states of the remaining pockets can affect barrier heights for ligand migration between two given pockets but also that the effect is not necessarily additive.

The Xe4↔Xe2 transition: Barriers for this transition are uniformly high. Except for the 1011 occupation state further relaxation and adaptation may be possible for scans in both directions. This is evidenced by the fact that for the Xe4→Xe2 direction with Xe in Xe2 ($r_c = 1$) is more stable for 0001, 1001, and 0011, whereas the reverse is true for moving Xe in the opposite direction Xe4←Xe2.

The Xe4↔DP transition: The occupation of neighboring pockets significantly lowered the ΔG_f for Xe4↔DP (bottom line in Figure 2) in 0101 (Fig. 2N), 1001 (Fig. 2O), and 1011 (Fig. 2P). Other than for the forward transition, ΔG_r decreased for 1001 and 1011 com-

pared with 0001. The activation barrier decreased from 4 kcal/mol in 0001 (Fig. 2M) to 1.1 kcal/mol in 1011 ($\Delta G_r = 5.7$ kcal/mol). However, occupation of only the Xe2 pocket (0101) destabilized the Xe4 pocket by ~ 1 kcal/mol and had no effect on ΔG_r . The activation barriers for reverse transitions feature late transition states ($r_c = 0.65$) with the barrier closer to DP for 0001, 0101, and 1011 states.

Overall, the Xe4 \leftrightarrow Xe2 transition is less likely to occur compared to all other transitions. The longer distance between these two pockets decreases the probability for this transition. Occupation of internal pockets can modulate barrier heights (0100 vs. 0101 for Xe2 \leftrightarrow Xe3) and the effect of pocket occupation does not need to be additive (compare ΔG for 0101, 1100, and 1101 for Xe2 \leftrightarrow Xe3).

3.2 Further Relaxation for the Xe4 \leftrightarrow DP Transition

For 0001 and 0101, the free energy of the states with Xe in pocket DP differs whether the transition is followed in the forward (black) or the reverse (red) direction, see Figure 2M and N. As was already seen for multiple independent US simulations for the Xe1 \rightarrow Xe2 transition, variations in barrier heights and relative stabilization can be expected for repeated scans of the same transition. To probe the relevance of additional relaxation along the reaction coordinate, Xe migration in 0101 was repeatedly followed in the forward (Xe4 \rightarrow DP) and reverse direction (DP \rightarrow Xe4). For this, the final structure of each scan was the starting geometry for the following scan in the opposite direction. Overall, 5 scans in the forward and in the reverse direction were carried out. The results are shown in Figure 4 with the forward PMFs as solid lines and those for the reverse scans as dashed lines in order black - blue - green - orange - indigo.

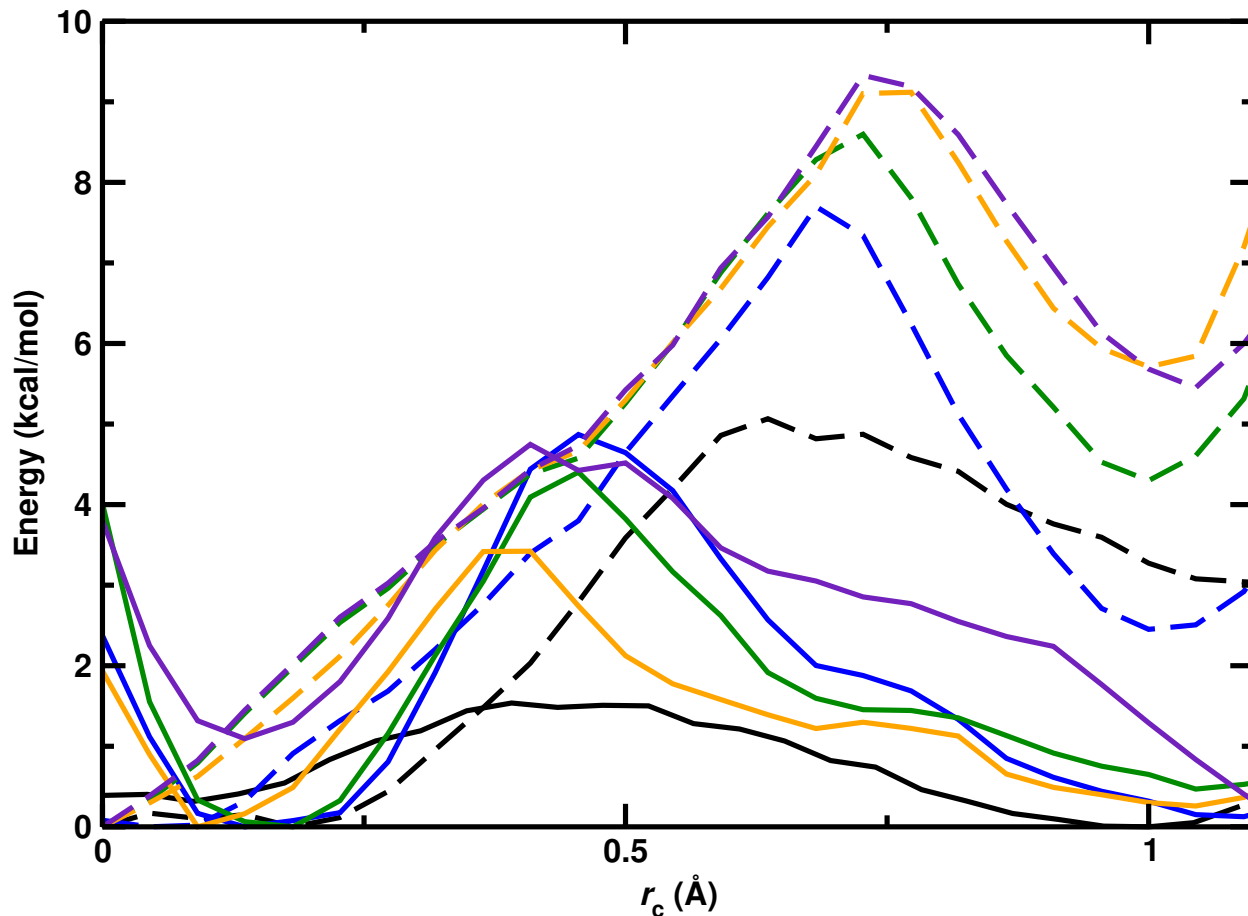


Figure 4: The PMF of the $\text{Xe4} \leftrightarrow \text{DP}$ transition for 0101. PMFs in the forward direction ($\text{Xe4} \rightarrow \text{DP}$) are the solid lines whereas the PMFs in the reverse direction ($\text{Xe4} \leftarrow \text{DP}$) are shown as dashed lines. The final structure of each scan is the starting point for the following scan in the opposite direction. The scan order is: black - blue - green - orange - indigo. The state with Xe in Xe4 ($r_c = 0$) is the zero of energy for all scans.

In the forward direction, the differential stabilization for Xe in both states was close to zero. However, the activation barriers increased from 1.5 kcal/mol to 4.87, 4.40, 3.42, and 4.74 kcal/mol for blue, green, orange, and indigo scans, respectively. Conversely, for the reverse scan Xe in DP ($r_c = 1$) is always higher in energy compared with Xe in Xe4 ($r_c = 0$). The differential stabilization changed from 3.0 to 2.5, 4.3, 5.8, and 5.5 kcal/mol for black, blue, green, orange, and indigo scans, respectively. In addition, the activation barriers changed from 1.30 to 5.24, 4.30, 3.41, and 3.87 kcal/mol for black, blue, green, orange, and indigo scans, respectively. These results show the importance of the initial configuration (see also

figure 3) as the structural (re)arrangements of nearby residues can promote or impede Xe migration. Furthermore, it is also demonstrated that the differential stabilization and activation barrier in the forward and reverse direction for given occupation state (here 0101) can depend on the direction in which the transition is probed.

The activation barriers found in the present work are largely consistent with previous studies. The DP→Xe4 for the 0001 transition has a barrier of 5.7 kcal/mol compared with 5.4 kcal/mol⁵² calculated for CO diffusion. Based on implicit sampling⁵³ barrier heights for Xe diffusion along different internal paths were determined. For the empty protein the barrier between DP and Xe4 is between 5 and 6 kcal/mol with the state with Xe in Xe4 lower in energy. Similarly, for Xe2→Xe1 in 0100, the calculated value of 1.5 kcal/mol is consistent with 1.4 kcal/mol calculated from meta-dynamics simulations using CO as the ligand.⁵⁴ Additional barriers were also determined from this approach but it was stated that the barrier heights were overestimated as a consequence of the implicit ligand sampling approach. On the other hand, the activation barrier of 4.8 kcal/mol found here for the Xe4→Xe2 transition in 0001 were somewhat higher compared to the previous studies 2.9⁵² and 2.7 kcal/mol.⁵⁴ When comparing with earlier efforts one should note that the barrier heights can depend on the definition of the reaction coordinate, and the initial structure/preparation of the system used for the simulations.

3.3 Unbiased Simulations

Multiple unbiased simulations were performed to compare with the free energy barriers from the US simulations, see Figure 2. For this, the transition times τ for the Xe2→Xe1 transition for 0101 occupation were determined from 2500 independent trajectories, each 1 ns in length. Out of those, in 329 runs the transition of interest occurred which corresponds to 13 % of the trajectories. The transition time is determined as the time difference between the start

of the simulation and the first time Xe was in the Xe1 pocket. Xe is considered to reside in the pocket when the distance between Xe and the center of the pocket is lower than 4 Å. The 4 Å threshold chosen due to the fact that 4 Å sphere would have volume of $\sim 256 \text{ Å}^3$ which is the volume of the empty Xe1 pocket.

The distribution of transition times is reported in the inset of Figure 3. The average transition time is ~ 500 ps which corresponds to a free energy difference of ~ 3.5 kcal/mol based on transition state theory, consistent with 2.5 kcal/mol from the umbrella sampling simulations, see Figure 2B. However, the actual transition times cover a range from 68 ps to 1 ns and the fact that there is a distribution of transition times is also reflected in the distribution of barrier heights that was found for the repeat US simulations in Figure 3.

The results in inset of Figure 3 show that there is not one specific transition time and that the values for τ do not follow a “simple” distribution, e.g. a Gaussian, because the underlying process is one that is rather characterized by “waiting times”, at least for short τ . This reflects the fact that depending on the initial configuration from which the simulation was started more or less structural arrangements and fluctuations are required to promote diffusion of Xe from the initial to the final pocket.

3.4 Correlated Motions from Dynamic Cross Correlation Maps

For a more atomistically refined picture regarding the underlying motions in the proteins, DCCMs provide a basis to determine the importance of transition direction and neighboring pocket occupation on the overall and site-specific dynamics. As the PMFs in Figure 2 show, the profile along the reaction coordinate between the initial and final state does not need to be symmetrical. Hence, the (local) protein dynamics accompanying a transition may differ in the forward and the reverse direction. This is indeed what is observed in the DCCM

maps. Such maps were constructed for specific transitions and occupations from US and from unbiased simulations and are discussed in the following.

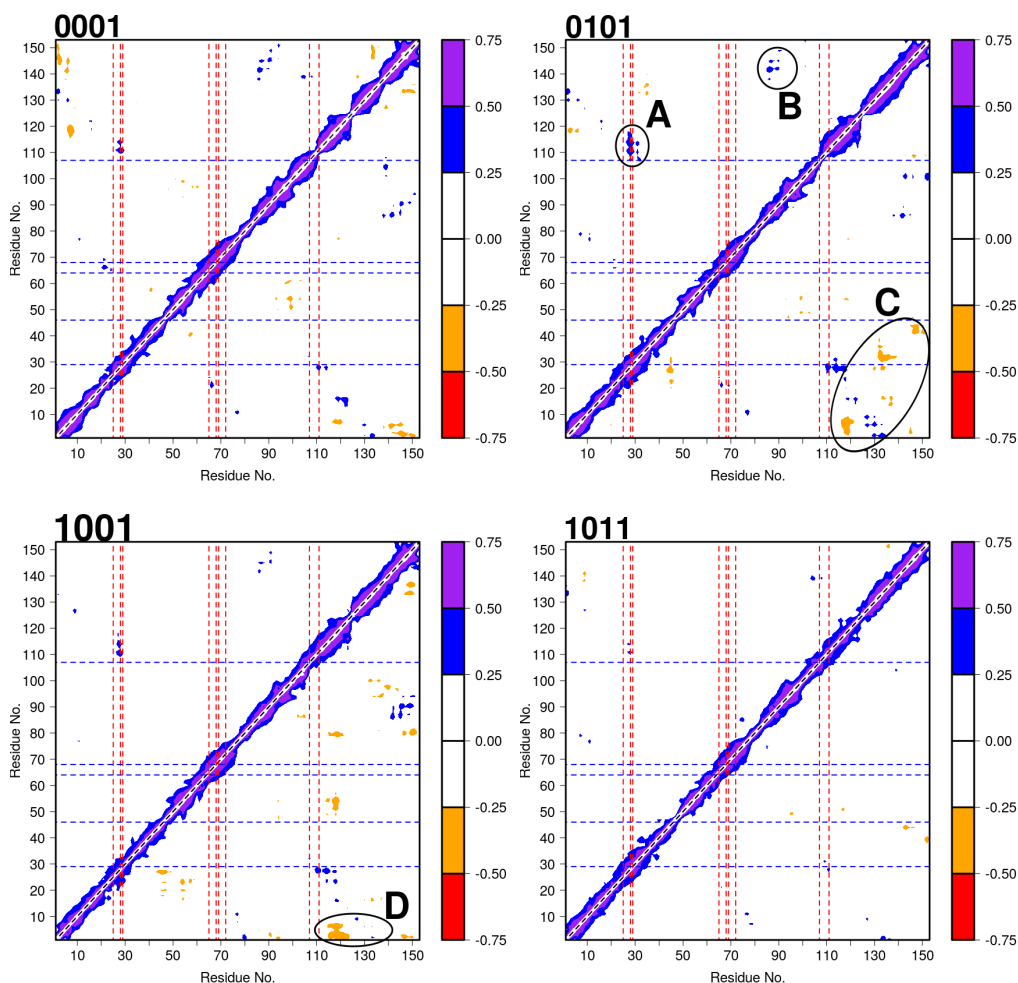


Figure 5: The DCCM of $\text{Xe4} \rightarrow \text{DP}$ (upper left triangle) and $\text{Xe4} \leftarrow \text{DP}$ (lower right triangle) transition in 0001, 0101, 1001, 1011. Vertical red lines indicate the residues that form the Xe4 pocket whereas horizontal blue lines indicate the residues that form the DP. Particular features in the maps are labeled from A to D with circles around them

For the $\text{Xe4} \leftrightarrow \text{DP}$ transition (for PMFs see Figure 2M to P and Figure 4) the motions in the reverse direction ($\text{Xe4} \leftarrow \text{DP}$; lower right triangles in Figure 5) compared with the forward direction ($\text{Xe4} \rightarrow \text{DP}$; upper left triangles in Figure 5) were more correlated/anti-correlated. Correlated motions can occur between residues adjacent to one another or through space, in

particular if the motion involves entire secondary structural motifs.

For the $\text{Xe4} \leftrightarrow \text{DP}$ transition, feature A in Figure 5 shows that correlated motions between the Gly25, Ile28, and Leu29 (part of pocket Xe4) with Ile107 to Ser117 are present for both forward and reverse directions. Ile107 is part of both, pockets Xe2 and Xe4. These residues are spatially close to each other and underscore coupling of Xe movement to the local protein dynamics. Correlated motions are also affected by the Xe occupation of neighboring pockets. Feature B in Figure 5, between Leu135 and Lys146 and Pro88 to Ser92 is present in 0001, 0101, and 1001 with different intensities, but not for 1011. For 1001 there are multiple correlated and anti-correlated motions for residues between [N-terminus,Lys50] and [Ala110,C-terminus] (Feature C). States with higher activation barrier (0001 and 0101, see Figure 2), showed more intense peaks in the DCCM maps. Anti-correlated motions between Val1 to Gln8 and Leu115 to Phe123 (feature D) shows spatially long-range motion correlation, which means that the effect of local dynamics can affect the global dynamics depending on the particular occupation state.

It is also of interest to analyze DCCMs as a function of simulation time which was done for the unbiased simulations for the $\text{Xe2} \rightarrow \text{Xe1}$ transition (0101 occupation), see Figure 6. The DCCMs were generated in 100 ps intervals by pooling and averaging over trajectories for which Xe migration occurred within the corresponding time interval. Hence, for 300 - 400 ps (upper right panel figure 6) all trajectories for which Xe migration occurred in this time window were analyzed together. Difference DCCMs (ΔDCCMs) show the differences between 0101 and the reference 0000 state. The upper left matrix shows DCCM for $\text{Xe2} \rightarrow \text{Xe1}$ transition whereas the lower right matrix is ΔDCCM for a given time interval and with 0000 as the reference state. For the DCCMs, three common features have been observed for all time intervals with varying intensities, A) Correlated motions between residues Val1 to Ile30 and 110 to 135 which are long-range interaction. B) Anti-correlated motions between

residues Arg45 to Lys62 and Ser92 to Tyr103 which are mid-range interactions, and C) Anti-correlated motions between residues Asp20 to Arg31 and Glu41 to Asp60. These features are labelled in Figure 6.

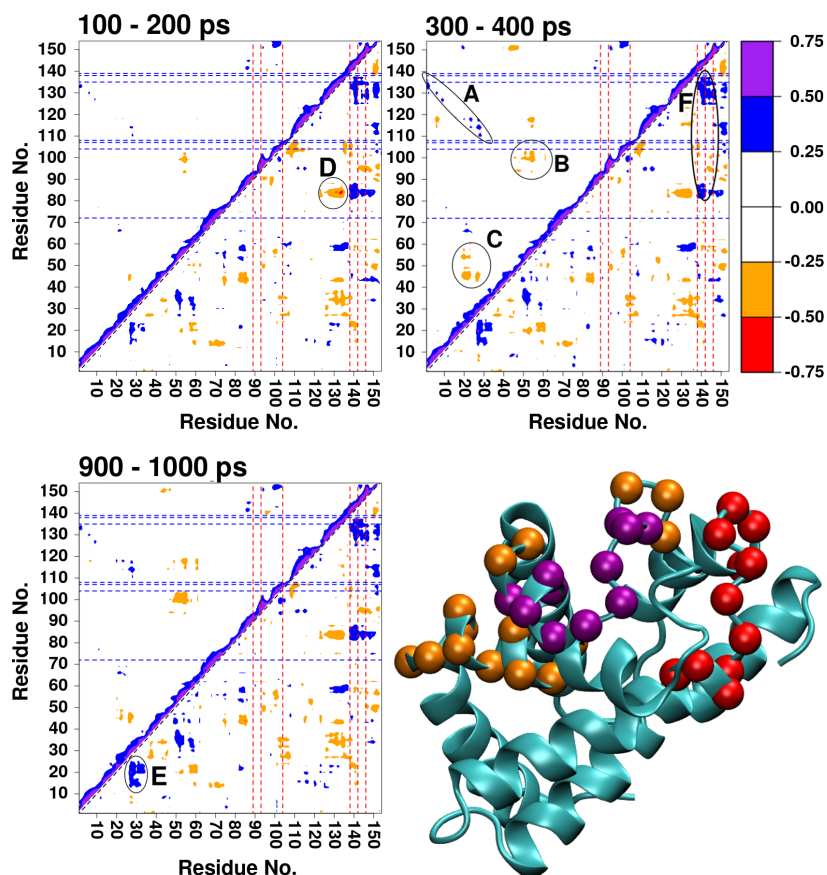


Figure 6: The DCCM from the 1 ns free dynamics simulations in which the Xe2→Xe1 transition is observed for 0101. The DCCM was generated at 100 ps intervals. The Upper matrix shows DCCM for Xe2→Xe1 transition whereas the lower matrix is Δ DCCM for a given time interval and the 0000 reference state. DCCMs correspond to transition times between 100 to 200 ps, 300 to 400 ps, and 900 to 1000 ps. Residue 154 is the Xe atom. Vertical red lines indicate the residues that form the Xe1 whereas horizontal blue lines indicate the residues that form the Xe2. Particular features in the maps are labeled from A to F with circles around them. Features B and C of DCCM visualized on myoglobin structure for Xe2→Xe1 in 0101. The color code is as follows: C_α of feature B (Ala19 to Leu29 and Phe43 to Ser58) orange, C_α of feature C (Phe46 to Lys56 and Ala94 to Leu104) is red and C_α that are part of both features is purple. The blue line emphasizes the correlated motions between given atoms.

Δ DCCMs show the structural effects induced by the Xe atom on the local structure around the Xe1 and Xe2 pockets and the global structure of the protein. Upon transition, correlated motions in myoglobin are significantly altered. Compared with the empty protein, strong correlated (feature D, $C_{ij} \geq 0.75$, see Figure 6) and anti-correlated (feature E, $C_{ij} \leq -0.75$, see Figure 6) motions are observed. No difference in correlation motions ($C_{ij} \geq 0.25$) been observed from N-terminus to Asp27. Further, Phe138, Ile142, Tyr146 of Xe1 and Leu135, Phe138, Arg139 of Xe2 show correlated motions in 0101 compared with the empty protein. In particular, residues Phe138, Ile142, Tyr146 of pocket Xe1 show correlated motions with residues Ala125 to Arg139 and His82 to Lys87 when considering the Δ DCCM maps. Strongly correlated motions involving residues Phe138 to the C-terminus were also found (see Figure 6, label F)

Overall DCCM and Δ DCCM show that correlated motions of the protein are subject to transition direction and neighboring pocket occupation upon Xe transition, as shown in Figure 5. The correlation/anti-correlation in residue motion accompanying transition of Xe between neighboring pockets and depending on occupation state are indicative of allostery. The results for the 0101 occupation suggest that insertion of xenon into the protein significantly decreased the correlated/anti-correlated motions compared with the empty protein.

4 Discussion

The present work determined the energetics for Xe migration pathways between neighboring docking sites in Mb from biased and unbiased MD simulations for different occupation states of the protein. Generally it was found that differential stabilization of the endpoints and barrier heights for Xe in the initial and final state can depend on both, occupation of the remaining docking sites and the direction in which the transition was scanned. Unbiased

simulations for one transition confirmed that barrier heights from biased simulations (here umbrella sampling) are representative. However, the distribution of transition times also showed that associating a single ΔG value to a given transition is not particularly meaningful from repeat US simulations for one transition and from the finding that transition times are distributed over 1 ns from unbiased simulations on the same time scale. In the following, a structural interpretation for specific transition paths is attempted and the results obtained are put in a broader context.

Structural interpretation for $Xe2 \rightarrow Xe1$ (0101) and for $Xe1 \rightarrow Xe2$ (1001): The activation barrier was lowered by 3 kcal/mol in the reverse transition of $Xe1 \leftrightarrow Xe2$ in 0101 compared to the forward transition in 1001, see Figure 2. The side-chains are investigated to understand the decrease in barrier heights as a function of local motions. Figure 7 shows the CoM position of the Phe138 side chain is analyzed on XY, XZ, and YZ planes for $Xe2 \rightarrow Xe1$ transition in 0101 (Top) $Xe1 \rightarrow Xe2$ transition 1001 (Bottom).

The results show that the side chain of Phe138 has two conformations (open and closed) for 1001 whereas it remains in the open conformation for 0101. The conformation in 0101 allows easier access for Xe to the Xe1 pocket, whereas switching between the open and closed conformations through side-chain rotation inhibits Xe mobility between the pockets in 1001. One should note that sampling distinct conformations based on the occupation state may be linked to allostery. Overall, Phe138 acts as a gate between Xe1 and Xe2 pockets. Features A, B, and C of the DCCM for the trajectories with transition times of 300 ps to 400 ps are shown in Figure 6. These features report on both neighboring and through-space correlations. Transition times of 300 to 400 ps correspond to ~ 3 kcal/mol activation barrier which is on-par with calculated 1D PMF for the given transition.

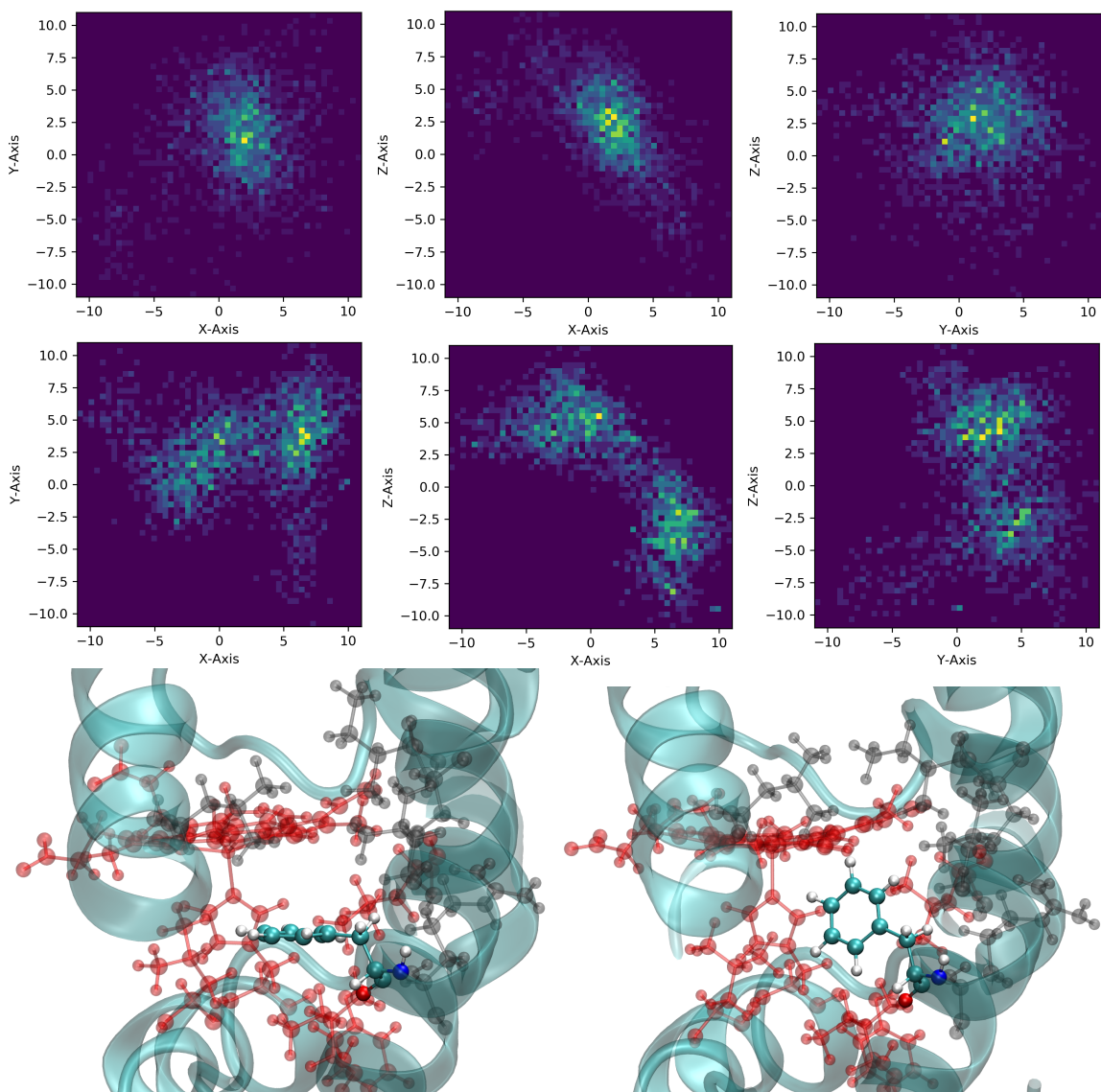


Figure 7: The center of mass position of the Phe138 side chain projected onto the xy , xz , and yz planes for the $\text{Xe2} \rightarrow \text{Xe1}$ transition in 0101 (Top) $\text{Xe1} \rightarrow \text{Xe2}$ transition 1001 (Middle). The data was extracted from the umbrella sampling simulations at the TS and for the two windows preceding and following the TS. The lighter color means higher probability and the two maxima shown in the middle row correspond to the open and close conformations of Phe138. In the bottom row the open (left) and closed (right) passage with residue Phe138 as the gate is shown. The red residues are part of pocket Xe1 (front) whereas black residues are part of pocket Xe2 (back).

The forward activation barrier for $\text{Xe1} \leftrightarrow \text{Xe2}$ in 1010 was 5 kcal/mol higher compared with the reverse barrier and the free the energy of the state with Xe in pocket Xe1 depends on whether the transition is followed in the forward (black) or the reverse (red) direction, see

Figure 2C. For a structural interpretation, the averaged protein structures of the first umbrella for the forward direction, and that for the last umbrella for the backward direction are considered, whereby both correspond to $r_c = 0$. The C_α atoms of the residues forming the Xe1 pocket (see Table 1) are superimposed. The root mean squared deviations (RMSD) of all heavy atoms of the residues forming the Xe1 pocket are collected in Table S2. Most importantly, the RMSD for all heavy atoms forming the Xe1 pocket was 1.33 Å, which shows that there are substantial structural differences even for the few residues forming the Xe1 pocket depending on whether the transition was scanned in forward or in reverse direction. The largest RMSD computed for all heavy atoms arises from Leu104 and Phe138 residues.

Correlated Motions Depending on Transition Time: The total correlation of a group of residues can be used to compare the strengths of dynamical coupling depending on the occupation state or depending on a particular time window of the simulations. For this, the correlation coefficients C_{ij} involving groups of residues i to j were added to determine $c_{ij} = 1/N \sum_{i=1}^n \sum_{j=1}^m C_{ij}$, where n and m are the numbers of residues over which a given feature extends, N is the total number correlation coefficient ($N = m \times n$). As an example for Feature B, correlation coefficients of Ala19 with Phe43 to Ser58 are summed; then coefficients of Asp20 with Phe43 to Ser58 are added to the previous summation; summations are continued until the coefficients of Leu29 with Phe43 to Ser58 added. Finally, total number is divided by N . For features B and C, c_{ij} presented as a function of time and reported in Figure S1. All c_{ij} between Ala19 to Leu29 and Phe43 to Ser58 for B, and Phe46 to Lys56 and Ala94 to Leu104 are summed and divided by the total number of residues for each feature to determine how the total correlation for a group of residues changes as a function of simulation time. For feature B there was an initial increase then it was stable until 0.8 ns, afterwards increase in magnitude to the initial values levels is observed. For feature C the total anti-correlation increased until 0.4 ns after which it stabilizes. Hence, depending on the group of residues considered the total correlation between participating residues can

also behave differently as a function of simulation time.

Analysis of pocket volumes: Another property that provides information about internal protein rearrangements is the volume of the internal cavities and their fluctuations along the ligand migration pathway. This was done for the Xe1 and Xe2 volumes along the Xe1 \leftrightarrow Xe2 transition pathway. The distribution of pocket volumes from the US simulations for Xe1 \rightarrow Xe2 as a function of reaction coordinate is shown in Figure 8. The filled circles are the median pocket volumes along the reaction coordinate, determined using the 50th percentile of the cumulative probability distribution, based on a kernel density estimation.

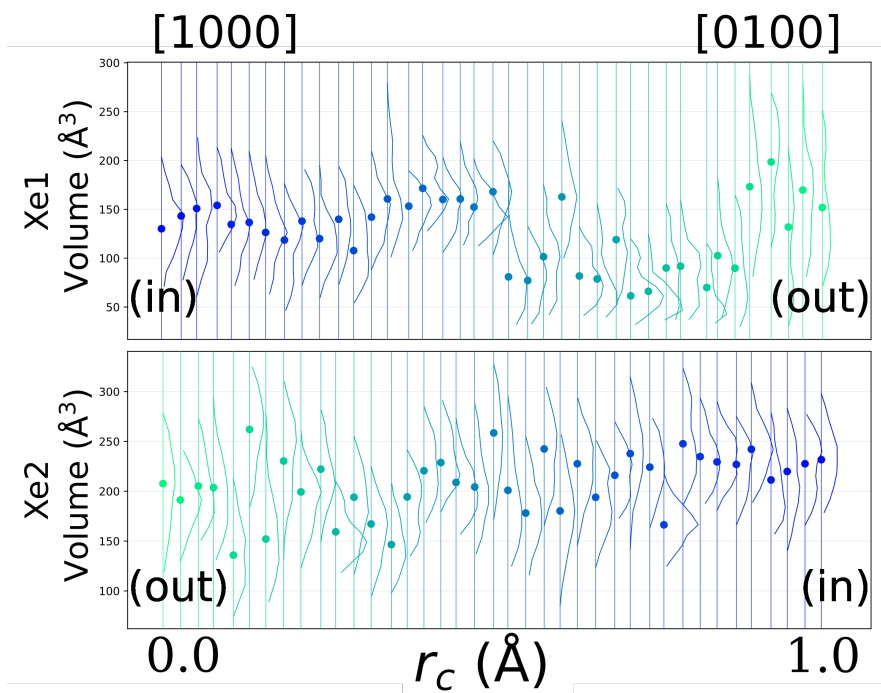


Figure 8: The volume of Xe1 and Xe2 for the Xe1 \rightarrow Xe2 transition starting for the 1000 state. (In) and (Out) refer to the Xe atom inside the initial (Xe1) pocket and the final (Xe2) pocket, respectively. The points are the median of the pocket volumes.

The distributions and the median volumes demonstrate that depending on the position of the xenon atom along the pathway the volumes of the pockets respond. The volume distributions are non-Gaussian, sometimes with more than one peak, and vary from one umbrella window to the next for each pocket considered. The average volume of the Xe1 pocket (top panel) first varies between 100 and 166 Å³ and sharply decreases by $\sim 50\%$ after $r_c > 0.5$ Å, when Xe leaves the Xe1 pocket, until $r_c = 0.8$ Å. After that, the Xe1 pocket volume returns to its initial value which was ~ 150 Å³. For the Xe2 pocket the average volume is ~ 200 Å³ but along the transition pathway the fluctuation around this value is $\sim \pm 50$ Å³. The volume of the Xe2 pocket decreases for the first part of the transition (green in Figure 8). The Xe2 pocket volume fluctuates more in $0.5 < r_c < 0.6$ Å region which corresponds to the “transition” region for Xe1 \leftrightarrow Xe2.

The DP \leftrightarrow Xe4 Transition: Physiologically, the DP to Xe4 transition is most relevant.^{17,18} The findings from repeat forward and reverse simulations (see Figure 4) indicate that Xe in DP is higher in energy compared with Xe in Xe4 by 4.22 kcal/mol on average. The free energy barrier separating the two states is 3.79 kcal/mol in the forward and 3.62 kcal/mol in the reverse direction on average. The differential stabilization in favour of Xe in Xe4 is consistent with flash photolysis experiments on CO in Mb which find spontaneous CO diffusion from docking site “B” to Xe4 on the nanosecond time scale.⁵⁵ Similarly, implicit ligand sampling simulations also found stabilization of Xe in Xe4 to be more favourable than in DP.⁵³ These comparisons provide independent validation of the present simulations.

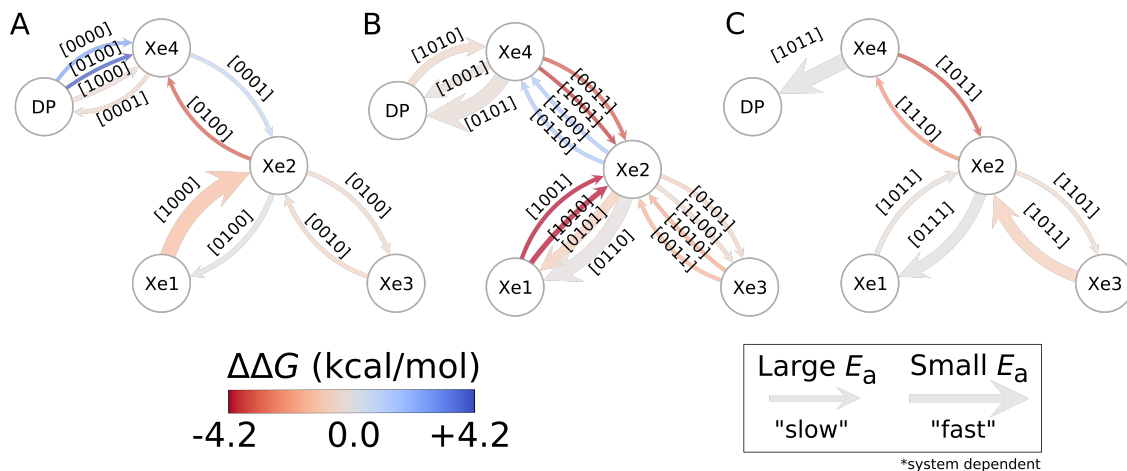


Figure 9: Network representation illustrating the transitions studied for systems with (A) one xenon atom, (B) two xenon atoms and (C) three xenon atoms occupying the protein. Arrows are colored by the difference in free energy between the initial and the final states and labelled by the initial occupation state (i.e. 1000 for $\text{Xe1} \rightarrow \text{Xe2}$). The size of the arrows is proportional to the ratio of rate constant for transitions, estimated using the Arrhenius equation at 300 K, assuming the same Arrhenius prefactor for all transitions, and can be compared between each of the three distinct occupancies.

State dependence on xenon transitions in Mb: Specific occupancies of internal pockets in myoglobin introduce correlation between distant sites of the protein. Network representations, as shown in Figure 9, provide an overarching view of all migration pathways considered. Nodes indicate the identity of the pockets as their associated residues are known through experiment. In such a directed graph, edges represent transitions which were analysed using their respective potential of mean forces to provide estimates of relative stabilization energies and barriers, see Table S1. For xenon migration in myoglobin, the occupied versus empty state of a particular pocket has a measurable impact on the kinetic and thermodynamic properties of the transitions, as seen in Figure 9. Transitions which require excess free energy to occur when only one xenon atom occupies the protein (Figure 9A), in DP to Xe4, and Xe4 to Xe2, can occur spontaneously when an additional xenon atom occupies either Xe1 or Xe3, respectively (Figure 9B). Hence, occupation of specific internal pockets can modulate energy barriers for a given transition path which also leads to changes in the relative kinetic rates. For instance, the forward transition between Xe1 to Xe2 is more kinetically favoured

when internal pockets are unoccupied (a factor of ~ 10 times faster than the reverse transition) and are slower in proportion to comparable transitions when an additional xenon atom is present in a distant pocket (approximately a factor of 20 times slower than the reverse transition, (Figure 9B)). The same trend is observed for this transition when 3 xenon atoms are occupying the protein (Figure 9C), where the reverse transition is also favoured.

5 Conclusion

In conclusion, both energetic and structural analyses were performed to better understand the molecular level characteristics of the ligand movements inside myoglobin and whether/how they relate to allostery. These analyses are further supported by the DCCMs, side-chain, and volume calculations. For a particular transition, the occupation of the neighboring pockets greatly affects both energetics and structural dynamics of the protein. The activation barriers and the relative stabilizations for the ligand in the initial and final pocket of a transition are distributed, rather than a single, discrete value, that depends on the sampled initial meta-stable state. Side-chain degrees of freedom were found to gate particular transition pathways, as is the case of Phe138. The dependence of barrier heights on occupation state and scan-direction suggest that non-local communication between different protein sites occurs which is a hallmark of allosteric control. The DCCMs, which characterize the correlated motions with the protein further support this interpretation. Finally, a network representation for all ligand migration pathways considered highlights the state dependence of thermodynamic and kinetic properties. The sum of all these observations, which are based on a molecular-level characterization of xenon migration and protein dynamics, indicate that Mb is an allosteric protein. This finding is also consistent with earlier work on Mb which proposed that Mb is an allosteric enzyme by pointing to the important role of the internal cavities to speed up bimolecular reactions by increasing the concentration of the

physiological ligands and by reducing or entirely eliminating competing reaction pathways.⁴⁴

6 Acknowledgments

The authors gratefully acknowledge financial support from the Swiss National Science Foundation through grant 200021-117810 and to the NCCR-MUST.

References

- (1) Connolly, M. L. Atomic size packing defects in proteins. *Int. J. Pept. Protein Res.* **1986**, *28*, 360–363.
- (2) Tilton, R. F.; Kuntz, I. D.; Petsko, G. A. Cavities in Proteins: Structure of a Metmyoglobin-Xenon Complex Solved to 1.9 Å. *Biochem.* **1984**, *23*, 2849–2857.
- (3) Luna, V. M.; Fee, J. A.; Deniz, A. A.; Stout, C. D. Mobility of Xe atoms within the oxygen diffusion channel of cytochrome *ba*₃ oxidase. *Biochem.* **2012**, *51*, 4669–4676.
- (4) Liu, L.; Quillin, M. L.; Matthews, B. W. Use of experimental crystallographic phases to examine the hydration of polar and nonpolar cavities in T4 lysozyme. *PNAS* **2008**, *105*, 14406–14411.
- (5) Quillin, M. L.; Wingfield, P. T.; Matthews, B. W. Determination of solvent content in cavities in IL-1 β using experimentally phased electron density. *PNAS* **2006**, *103*, 19749–19753.
- (6) Eriksson, A. E.; Baase, W. A.; Zhang, X.-J.; Heinz, D. W.; Blaber, M.; Baldwin, E. P.; Matthews, B. W. Response of a protein structure to cavity-creating mutations and its relation to the hydrophobic effect. *Science* **1992**, *255*, 178–183.

- (7) Gabellieri, E.; Balestreri, E.; Galli, A.; Cioni, P. Cavity-creating mutations in *Pseudomonas aeruginosa* azurin: effects on protein dynamics and stability. *Biophys. J.* **2008**, *95*, 771–781.
- (8) Ohmura, T.; Ueda, T.; Ootsuka, K.; Saito, M.; Imoto, T. Stabilization of hen egg white lysozyme by a cavity-filling mutation. *Phys. Scr.* **2001**, *10*, 313–320.
- (9) Marcos, E.; Basanta, B.; Chidyausiku, T. M.; Tang, Y.; Oberdorfer, G.; Liu, G.; Swapna, G.; Guan, R.; Silva, D.-A.; Dou, J. et al. Principles for designing proteins with cavities formed by curved β sheets. *Science* **2017**, *355*, 201–206.
- (10) Milani, M.; Pesce, A.; Ouellet, Y.; Dewilde, S.; Friedman, J.; Ascenzi, P.; Guertin, M.; Bolognesi, M. Heme-ligand tunneling in group I truncated hemoglobins. *J. Biol. Chem.* **2004**, *279*, 21520–21525.
- (11) Cazade, P. A.; Meuwly, M. Oxygen migration pathways in NO-bound truncated hemoglobin. *ChemPhysChem* **2012**, *13*, 4276–4286.
- (12) Brunori, M.; Vallone, B. Neuroglobin, seven years after. *Cell. Mol. Life Sci.* **2007**, *64*, 1259–1268.
- (13) Kriegl, J. M.; Bhattacharyya, A. J.; Nienhaus, K.; Deng, P.; Minkow, O.; Nienhaus, G. U. Ligand binding and protein dynamics in neuroglobin. *Proc. Natl. Acad. Sci.* **2002**, *99*, 7992–7997.
- (14) Lutz, S.; Nienhaus, K.; Nienhaus, G. U.; Meuwly, M. Ligand migration between internal docking sites in photodissociated carbonmonoxy neuroglobin. *J. Phys. Chem. B* **2009**, *113*, 15334–15343.
- (15) Nienhaus, K.; Lutz, S.; Meuwly, M.; Nienhaus, G. U. Structural identification of spectroscopic substates in neuroglobin. *ChemPhysChem* **2010**, *11*, 119–129.

- (16) De Sanctis, D.; Dewilde, S.; Pesce, A.; Moens, L.; Ascenzi, P.; Hankeln, T.; Burmester, T.; Bolognesi, M. Mapping protein matrix cavities in human cytoglobin through Xe atom binding. *Biochem. Biophys. Res. Commun.* **2004**, *316*, 1217–1221.
- (17) Olson, J. S.; Soman, J.; Phillips, G. N. Ligand pathways in myoglobin: A review of trp cavity mutations. *IUBMB Life* **2007**, *59*, 552–562.
- (18) Scott, E. E.; Gibson, Q. H.; Olson, J. S. Mapping the Pathways for O₂ entry Into and exit from myoglobin. *J. Biol. Chem.* **2001**, *276*, 5177–5188.
- (19) Kachalova, G. S.; Popov, A. N.; Bartunik, H. D. A steric mechanism for inhibition of CO binding to heme proteins. *Science* **1999**, *284*, 473–476.
- (20) Nishihara, Y.; Sakakura, M.; Kimura, Y.; Terazima, M. The escape process of carbon monoxide from myoglobin to solution at physiological temperature. *J. Am. Chem. Soc.* **2004**, *126*, 11877–11888.
- (21) Monod, J.; Jacob, F. General conclusions: teleonomic mechanisms in cellular metabolism, growth, and differentiation. Cold Spring Harbor symposia on quantitative biology. 1961; pp 389–401.
- (22) Pauling, L. The oxygen equilibrium of hemoglobin and its structural interpretation. *Proc. Nat. Acad. Sci. USA* **1935**, *21*, 186–191.
- (23) Koshland Jr, D. E.; Némethy, G.; Filmer, D. Comparison of experimental binding data and theoretical models in proteins containing subunits. *Biochem.* **1966**, *5*, 365–385.
- (24) Tsai, C.-J.; Del Sol, A.; Nussinov, R. Allostery: absence of a change in shape does not imply that allostery is not at play. *J. Mol. Biol.* **2008**, *378*, 1–11.
- (25) Changeux, J.-P.; Edelstein, S. J. Allosteric mechanisms of signal transduction. *Science* **2005**, *308*, 1424–1428.

- (26) Link, H.; Christodoulou, D.; Sauer, U. Advancing metabolic models with kinetic information. *Curr. Opin. Biotechnol.* **2014**, *29*, 8–14.
- (27) Cui, Q.; Karplus, M. Allostery and cooperativity revisited. *Protein Sci.* **2008**, *17*, 1295–1307.
- (28) Motlagh, H. N.; Wrabl, J. O.; Li, J.; Hilser, V. J. The ensemble nature of allostery. *Nature* **2014**, *508*, 331–339.
- (29) Guo, J.; Zhou, H.-X. Protein Allostery and Conformational Dynamics. *Chem. Rev.* **2016**, *116*, 6503–6515.
- (30) Strotz, D.; Orts, J.; Kadavath, H.; Friedmann, M.; Ghosh, D.; Olsson, S.; Chi, C. N.; Pokharna, A.; Güntert, P.; Vögeli, B. et al. Protein Allostery at Atomic Resolution. *Angew. Chem. Int. Ed.* **2020**, *59*, 22132–22139.
- (31) Sethi, A.; Eargle, J.; Black, A. A.; Luthey-Schulten, Z. Dynamical networks in tRNA:protein complexes. *Proc. Nat. Acad. Sci. USA* **2009**, *106*, 6620–6625.
- (32) Chennubhotla, C.; Bahar, I. Markov propagation of allosteric effects in biomolecular systems: application to GroEL–GroES. *Mol. Syst. Biol.* **2006**, *2*, 36.
- (33) Atilgan, A. R.; Akan, P.; Baysal, C. Small-World Communication of Residues and Significance for Protein Dynamics. *Biophys. J.* **2004**, *86*, 85–91.
- (34) Hayatshahi, H. S.; Ahuactzin, E.; Tao, P.; Wang, S.; Liu, J. Probing Protein Allostery as a Residue-Specific Concept via Residue Response Maps. *J. Chem. Inf. Model.* **2019**, *59*, 4691–4705.
- (35) Brooks, B. R.; Bruccoleri, R. E.; Olafson, B. D.; States, D. J.; Swaminathan, S.; Karplus, M. CHARMM: A program for macromolecular energy, minimization, and dynamics calculations. *J. Comput. Chem.* **1983**, *4*, 187–217.

- (36) Cohen, J.; Arkhipov, A.; Braun, R.; Schulten, K. Imaging the migration pathways for O₂, CO, NO, and Xe inside myoglobin. *Biophys. J.* **2006**, *91*, 1844–1857.
- (37) Hairer, E.; Lubich, C.; Wanner, G. Geometric numerical integration illustrated by the Störmer–Verlet method. *Acta Numer.* **2003**, *12*, 399–450.
- (38) Ryckaert, J.-P.; Ciccotti, G.; Berendsen, H. J. Numerical integration of the cartesian equations of motion of a system with constraints: molecular dynamics of n-alkanes. *J. Comput. Phys.* **1977**, *23*, 327–341.
- (39) Steinbach, P. J.; Brooks, B. R. New spherical-cutoff methods for long-range forces in macromolecular simulation. *J. Comput. Chem.* **1994**, *15*, 667–683.
- (40) Tilton, R. F.; Singh, U. C.; Weiner, S. J.; Connolly, M. L.; Kuntz, I. D.; Kollman, P. A.; Max, N.; Case, D. A. Computational studies of the interaction of myoglobin and xenon. *J. Mol. Biol.* **1986**, *192*, 443–456.
- (41) Bossa, C.; Amadei, A.; Daidone, I.; Anselmi, M.; Vallone, B.; Brunori, M.; Nola, A. D. Molecular dynamics simulation of sperm whale myoglobin: Effects of mutations and trapped CO on the structure and dynamics of cavities. *Biophys. J.* **2005**, *89*, 465–474.
- (42) Park, S. Y.; Yokoyama, T.; Shibayama, N.; Shiro, Y.; Tame, J. R. 1.25 Å resolution crystal structures of human hemoglobin in the oxy, deoxy and carbonmonoxy forms. *J. Mol. Biol.* **2006**, *360*, 690–701.
- (43) Anselmi, M.; Nola, A. D.; Amadei, A. The kinetics of ligand migration in crystallized myoglobin as revealed by molecular dynamics simulations. *Biophys. J.* **2008**, *94*, 4277–4281.
- (44) Frauenfelder, H.; McMahon, B. H.; Austin, R. H.; Chu, K.; Groves, J. T. The role of structure, energy landscape, dynamics, and allostery in the enzymatic function of myoglobin. *Proc. Nat. Acad. Sci. USA* **2001**, *98*, 2370–2374.

- (45) Anselmi, M.; Di Nola, A.; Amadei, A. The effects of the L29F mutation on the ligand migration kinetics in crystallized myoglobin as revealed by molecular dynamics simulations. *Proteins* **2011**, *79*, 867–879.
- (46) Kumar, S.; Rosenberg, J. M.; Bouzida, D.; Swendsen, R. H.; Kollman, P. A. The weighted histogram analysis method for free-energy calculations on biomolecules. I. The method. *J. Comput. Chem.* **1992**, *13*, 1011–1021.
- (47) Souaille, M.; Roux, B. Extension to the Weighted Histogram Analysis Method: Combining Umbrella Sampling with Free Energy Calculations. *Comput. Phys. Commun.* **2001**, *135*, 40–57.
- (48) Ichiye, T.; Karplus, M. Collective motions in proteins: a covariance analysis of atomic fluctuations in molecular dynamics and normal mode simulations. *Proteins: Struct. Funct. Genet.* **1991**, *11*, 205–217.
- (49) Arnold, G. E.; Ornstein, R. L. Molecular dynamics study of time-correlated protein domain motions and molecular flexibility: cytochrome P450BM-3. *Biophys. J.* **1997**, *73*, 1147–1159.
- (50) Grant, B. J.; Rodrigues, A. P.; ElSawy, K. M.; McCammon, J. A.; Caves, L. S. Bio3d: an R package for the comparative analysis of protein structures. *Bioinformatics* **2006**, *22*, 2695–2696.
- (51) Laskowski, R. A. SURFNET: A program for visualizing molecular surfaces, cavities, and intermolecular interactions. *J. Mol. Graph.* **1995**, *13*, 323–330.
- (52) Ceccarelli, M.; Anedda, R.; Casu, M.; Ruggerone, P. CO escape from myoglobin with metadynamics simulations. *Proteins: Struct. Funct. Genet.* **2008**, *71*, 1231–1236.
- (53) Cohen, J.; Arkhipov, A.; Braun, R.; Schulten, K. Imaging the migration pathways for O₂, CO, NO, and Xe inside myoglobin. *Biophys. J.* **2006**, *91*, 1844–1857.

- (54) Nishihara, Y.; Hayashi, S.; Kato, S. A search for ligand diffusion pathway in myoglobin using a metadynamics simulation. *Chem. Phys. Lett.* **2008**, *464*, 220–225.
- (55) Schotte, F.; Lim, M.; Jackson, T. A.; Smirnov, A. V.; Soman, J.; Olson, J. S.; Phillips, G. N.; Wulff, M.; Anfinsen, P. A. Watching a protein as it functions with 150-ps time-resolved x-ray crystallography. *Science* **2003**, *300*, 1944–1947.

Supporting Information: “Interaction at a Distance: Xenon Migration in Mb”

Haydar Taylan Turan, Eric Boittier and Markus Meuwly*

Department of Chemistry, University of Basel, Klingelbergstrasse 80 , CH-4056 Basel, Switzerland.

E-mail: m.meuwly@unibas.ch

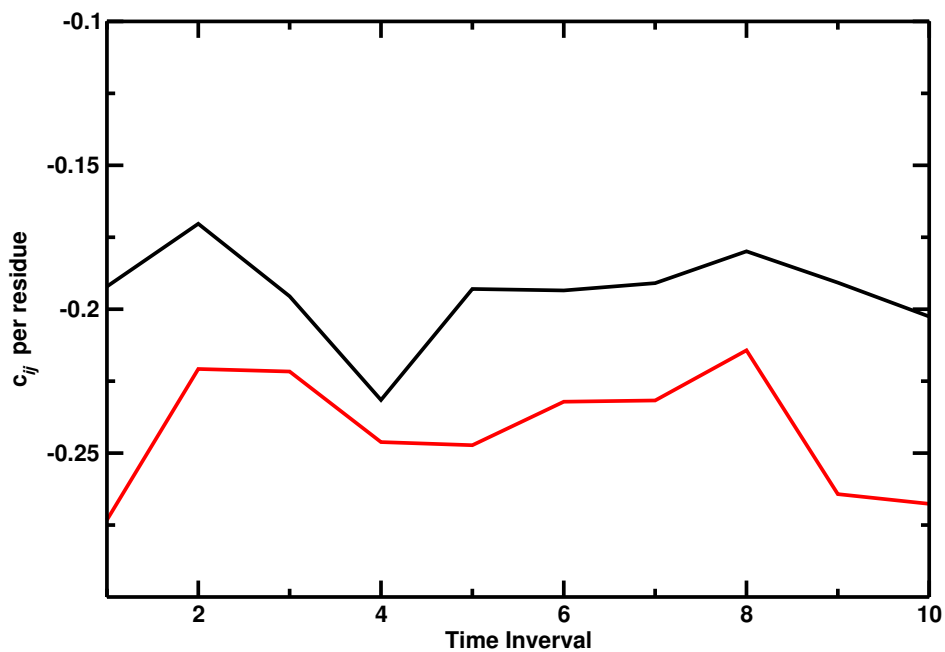


Figure S1: Cumulative correlation coefficients c_{ij} per residue of B (black) and C (red) features from DCCMs for Xe2→Xe1 in 0101. The B feature consists of the residues of Ala19 to Leu29 and Phe43 to Ser58, The C feature consists of the residues of Phe46 to Lys56 and Ala94 to Leu104.

Table S1: The activation energies (E_a) and thermodynamic parameter ($\Delta\Delta G$) from Figure 2 for forward and reverse transitions, for each system where N_{Xe} is the number of xenon atoms inside the protein. ΔG_{P_1} and ΔG_{P_2} represent the free energy for the starting and terminal pocket during the transition, respectively. Units for free energies are in kcal/mol.

N_{Xe}	State	P_1	P_2	ΔG_{P_1}	ΔG_{P_2}	E_a	$\Delta\Delta G$
1	0000	DP	Xe4	0.0	2.4	5.7	-2.4
1	0001	Xe4	Xe2	0.0	0.8	8.9	-0.8
1	0001	Xe4	DP	0.6	0.0	3.2	0.6
1	0010	Xe3	Xe2	0.6	0.0	2.5	0.6
1	0100	Xe2	Xe1	0.1	0.0	1.8	0.1
1	0100	Xe2	Xe3	0.5	0.0	2.5	0.5
1	0100	Xe2	Xe4	3.4	0.0	4.5	3.4
1	0100	DP	Xe4	0.0	4.1	5.4	-4.1
1	1000	Xe1	Xe2	1.4	0.0	0.6	1.4
1	1000	DP	Xe4	0.3	0.0	2.1	0.3
2	0011	Xe3	Xe2	1.6	0.0	4.4	1.6
2	0011	Xe4	Xe2	3.4	0.0	4.5	3.4
2	0101	Xe2	Xe1	0.9	0.0	1.6	0.9
2	0101	Xe2	Xe3	0.8	0.0	4.5	0.8
2	0101	Xe4	DP	0.3	0.0	1.2	0.3
2	0110	Xe2	Xe1	0.1	0.0	1.3	0.1
2	0110	Xe2	Xe4	0.0	1.5	9.3	-1.5
2	1001	Xe1	Xe2	4.2	0.0	3.0	4.2
2	1001	Xe4	Xe2	3.9	0.0	4.7	3.9
2	1001	Xe4	DP	0.2	0.0	1.8	0.2
2	1010	Xe1	Xe2	4.2	0.0	2.4	4.2
2	1010	Xe3	Xe2	1.8	0.0	4.1	1.8
2	1010	DP	Xe4	0.5	0.0	1.9	0.5
2	1100	Xe2	Xe3	0.5	0.0	3.3	0.5
2	1100	Xe2	Xe4	0.0	1.5	9.3	-1.5
3	0111	Xe2	Xe1	0.1	0.1	1.4	0.0
3	1011	Xe1	Xe2	0.2	0.0	2.5	0.2
3	1011	Xe3	Xe2	0.8	0.0	1.3	0.9
3	1011	Xe4	Xe2	3.5	0.0	5.7	3.5
3	1011	Xe4	DP	0.0	0.0	1.1	0.0
3	1101	Xe2	Xe3	0.4	0.0	3.4	0.4
3	1110	Xe2	Xe4	2.3	0.0	7.3	2.3

Table S2: The root mean square displacement (RMSD) in Å for Xe1 and the residues which form the Xe1 pocket for the Xe1 \leftrightarrow Xe2 transition. The average structure of Xe1 for the first umbrella of the forward direction, and for the last umbrella of the backward direction is compared. Both of these averaged structures correspond to $r_c = 0$, for their respective directions. The C $_{\alpha}$ of the residues forming Xe1 pocket are superimposed. The RMSD of the heavy atoms of Xe1 pocket is presented.

Residue	RMSD
Leu89	1.25
His93	0.71
Leu104	1.74
Phe138	1.90
Ile142	1.21
Tyr146	0.68
Xe1	1.33